Mapping birefringence in three dimensions using polarized light field microscopy: the case of the juvenile clamshell

M.T. TRAN*,† (iD) & R. OLDENBOURG*,† (iD)

*Marine Biological Laboratory, Woods Hole, Massachusetts, U.S.A.

†Physics Department, Brown University, Providence, Rhode Island, U.S.A.

Summary

We report methods to generate three-dimensional maps of birefringence, its position and orientation in juvenile shells of the Atlantic hard clamshell (*Mercenaria mercenaria*). For measuring the retardance and optic axis orientation of curved shell surfaces in three dimensions, we developed enhanced acquisition and processing algorithms and combined results from conventional and light field imaging approaches to reconstruct the three-dimensional shell shape and its anisotropic optical properties. Our work represents the first successful attempt to generate such maps at a spatial resolution of about 2 μm and angular steps of about 9° in terms of the inclination angles of the optic axis. The maps of clamshell birefringence provide structural insights into the early mineralization during juvenile clamshell development.

Introduction

Recently, we combined light field imaging and the liquid crystal based polarized light microscope (LC-PolScope) into the light field LC-PolScope that combines both orthoscopic and conoscopic observations into a single measurement process. In a first application, we analysed the birefringence of thin stratified films of polycrystalline calcite (Oldenbourg, 2008). Building on these results, we are now extending the technique to observe and analyse the three-dimensional (3D) geometric shape and optical properties of juvenile shells of the Atlantic hard clamshell, *Mercenaria mercenaria*, a thicker and more complex shape than a thin, stratified film.

The shells of bivalve molluscs like the hard clamshell are composed of calcium carbonate crystals in the form of calcite and/or aragonite, both of which exhibit strong birefringence. Juvenile shells of *M. mercenaria*, 2–4 days after fertilization, resemble a bent, thin, crystalline sheet, in which the orientation of the optic axis of the underlying crystal structure varies sys-

tematically with the position in the sheet (Tiwari & Gallager, 2003). Hence, these juvenile shells represent a birefringent structure that is well suited to further develop polarized light field imaging. Our results also provide benchmark and analysis approaches that relate optical properties of juvenile shells to their morphology that can be exploited for monitoring the health and development of bivalve aquacultures.

In the following sections, we describe the microscopes used and the methods to clean, prepare and manipulate samples, including epitaxial crystal growth to reveal the morphology and orientation of calcium carbonate crystals inside the shells. The epitaxial crystal growth is examined by scanning electron microscopy (SEM), and the 3D shape of cleaned shells is reconstructed by two different methods, conventional bright field microscopy and light field microscopy. The polarized light analysis using the light field LC-PolScope reveals the optical anisotropy and 3D orientation of its optic axis and their relationship to the morphology of the shell. Finally, the new light field LC-PolScope is applied to estimate the shell's thickness and its relationship to the shell's age. The results are compared with measurements using traditional techniques.

Materials and methods

Preparation of shells for microscopy

In our experiments, we examined 3-day-old hard clam embryos from the Aquacultural Research Corporation (ARC hatchery, Dennis, MA, USA). First, a batch of embryos were fixed with 2% formalin (Fisher Scientific, Pittsburgh, Pennsylvania, USA). Then the batches were transferred to 10%, 30%, 50% and 70% ethanol, consecutively, rinsed with deionized water ten times, and soaked for 6 h in 8.25% sodium hypochloride (NaClO) bleach solution to remove organic materials. Finally, the larval shells were washed 10 times in deionized water and stored in 70% ethanol.

For microscopic observations, a small amount of shells, which had collected in the bottom precipitate, was transferred onto a cover slip and left to dry completely.

Correspondence to: Mai T. Tran, Marine Biological Laboratory, 7 MBL Street, Woods Hole, MA 02543, U.S.A. Tel: +1-508-289-7426; fax: (508)-289-7900; e-mail: mtran@mbl.edu

For imaging in the scanning electron microscope, the dried shells were either covered with a thin platinum film, or placed directly into the SEM sample chamber without a conducting layer. For optical microscopy, the dried shells were immersed in oil ($n_{medium} = 1.52$) and sandwiched between a microscope slide and a cover slip and sealed with nail polish.

Epitaxial crystal growth on juvenile clamshells

After fixing and removing organic materials, a small batch of shells was suspended for 3 days in marine biological laboratory (MBL) artificial seawater with saturated sodium bicarbonate ($NaHCO_3$) to promote the epitaxial growth of calcium carbonate crystals on the shells' surface. The treated shells were washed many times with distilled water and were dehydrated overnight for SEM imaging.

Light field LC-PolScope

A bright field microscope and polarized light microscope such as the LC-PolScope can be easily converted into isotropic and polarized light field microscopes by exchanging the regular camera with a light field camera (Levoy et al., 2006). In the light field camera (Figure 2), there is a microlens array, which is placed at the image plane of the main lens, while the traditional detector array is placed in the focal plane 2.5 mm behind the microlens array. This microlens array allows the sensor to record additional information about the incoming rays of light, including their intensities and directions.

In our prototype, shown as a schematic in Figure 1, the universal compensator was fabricated by Meadowlark Optics Inc. (Frederick, CO, USA). The microlens array of the light field camera has a 125 μm pitch and consists of square microlenses with a focal length of 2.5 mm (Adaptive Optics Associates, now Northrop Grumman Mission Systems, Cambridge, MA, USA). The back focal plane of the microlens array is projected by a 1:1 relay lens onto a 2048 × 2048 pixel monochrome CCD camera (Retiga, 4000R, QImaging, Surrey BC, Canada; the size of a pixel is 7.4 × 7.4 μm). The relay lens was put together from two AF Nikkor 50 mm f/1.4D lenses (Nikon, Melville, NY, USA). The relay lens conveniently increases the required space between the microlens array and the camera sensor, which enables an easy conversion between conventional camera and light field camera.

Results

Three-dimensional shape reconstruction

In a first step towards mapping the 3D optical anisotropy of hard clamshells, we reconstructed the 3D shape of the shell using a bright field microscope setup without any polarizing components. In this paper, two methods were applied to build up a 3D model of the shell. First, the traditional method uses a bright field microscope and a conventional camera to image the absorption or attenuation of light that has passed through the shell. Since the hard clamshell material absorbs and scatters light, its shape can be reconstructed from a series of focal sections using high resolution optics (Fig. 3A). In doing so, we neglected the small mismatch in refractive index between the oil ($n = 1.52$) that surrounds the shell and the shell material ($n_o = 1.53$, $n_e = 1.68$). Assuming an average refractive index mismatch of 0.1, we underestimated the thickness of the shell by about 4%. Hence, we ignored this refraction effect. By identifying the shell's outer and inner surface in each slice by visual inspection (Fig. 4A), a model of the shell can be drawn and even 3D printed (Fig. 5D). Second, while using the same optical setup, we replaced the conventional camera with a light field camera to capture the shell's 3D distribution of absorption/scattering centres in a single snapshot (Fig. 3B). This light field image needs to be processed further to create optical sections or different perspective views of the shell. Here, the deconvolution method described in Broxton et al. (2013) was utilized to reconstruct a 3D model of the shell from its light field image.

Figure 4 illustrates reconstructed cross sections, which correspond to optical sections through the shell recorded at different focal planes (z-sections) and comparing corresponding z-sections obtained by conventional, high resolution bright field imaging (Fig. 4A) and by deconvolving the light field image (Fig. 3B). Each conventional optical section contains image details at high spatial frequencies that represent the shell's cross section at that focal plane, as pointed out by the green outline in the right most panel of Figure 4(A). Blurred image features outside the outlined cross section that appear as a black ring represent shell portions that are out of focus. Depending on the optical section, out of focus features can be more dominant in the image than the subtle, but detailed in focus features. By contrast, the optical sections reconstructed from the light field image do not contain fine absorption details from inside the cross section, but present the in focus part of the shell's cross section at lower resolution without dominant out of focus features. Hence, as expected, while the light field method does not have as good an in focus resolution as traditional imaging, this method paired with proper deconvolution largely removes out of focus features and allows the reconstruction of the 3D shape of the shell. Moreover, with light field imaging we can reconstruct the entire volume by recording a single image without moving the stage or specimen. Therefore, the method will be advantageous when analysing dynamic scenes.

The series of optical sections can be used to reconstruct the inner and outer shell surface and calculate the normal angles and thickness of the shell. In Figure 5, two vertical cross sections are shown in panels A and B, reconstructed from optical sections that were sliced along the green and red lines in Figure 5(C). The blue arrows present the normal vectors at points of the shell's surface. In particular, the thickness of the shell parallel to its normal is calculated by the product
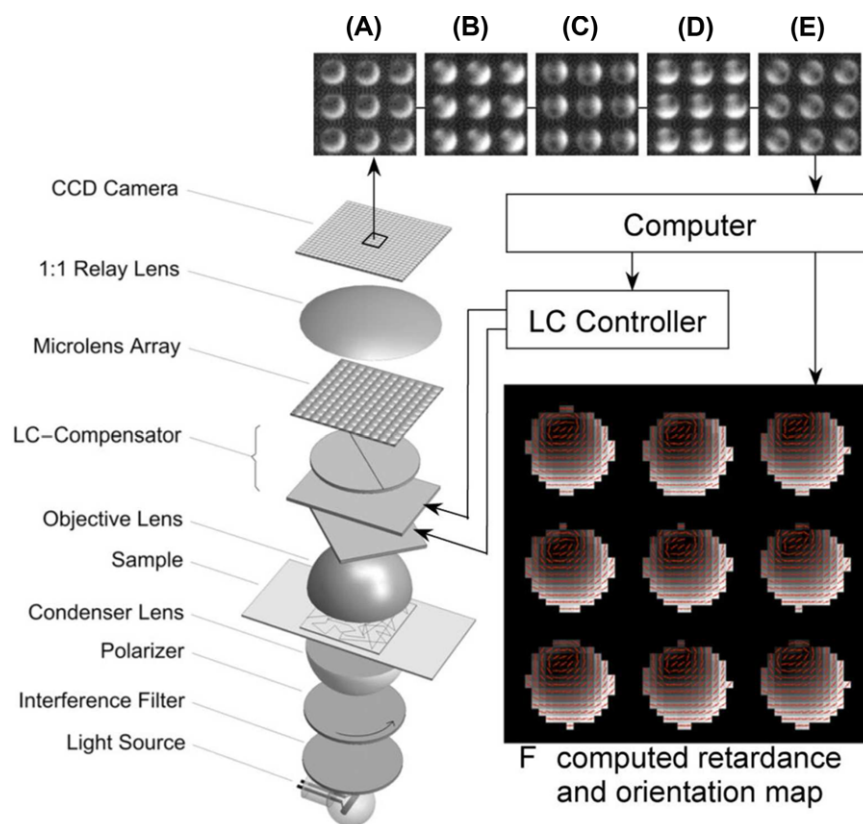
Fig. 1. Schematic of light field LC-PolScope including the optical setup, image acquisition and processing components. The optical parts include the light source, interference band pass filter, left circular polarizer, condenser lens, sample, objective lens, universal compensator, microlens array (placed in the objective lens' image plane), and a 1:1 relay lens. (A–E) Complete analysis of the polarized light field requires five raw images, corresponding to five settings of the LC compensator. The computer synchronizes the raw image acquisition with the compensator settings using a serial connection to the liquid crystal controller. (F) Based on the raw intensity images, the computer calculates a retardance and an orientation map, shown here as a composite image with red lines indicating the slow axis orientation. Reprinted from Oldenbourg (2008).
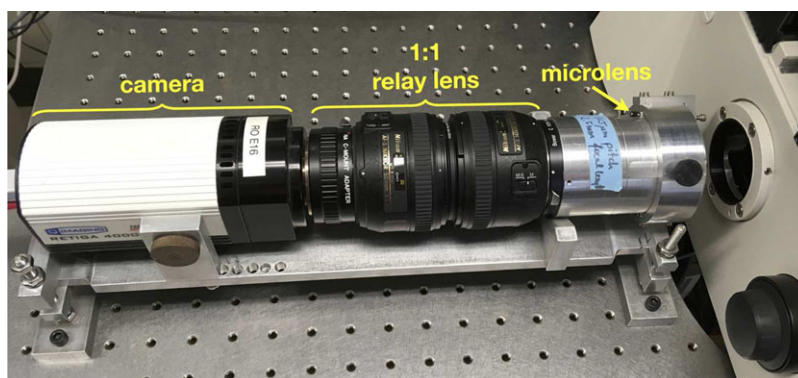

Fig. 2. The light field camera includes a microlens array at the image plane, a 1:1 relay lens and conventional CCD camera (QImaging Retiga 4000R).

of the thickness retrieved from the horizontal optical sections and the cosine of the normal angle. For example, the cross section near the top plane of the shell is shown in Figure 6, where the normal of the shell is inclined by 81° to the focus plane, as determined in Figure 5(B). Using the edge detection function in ImageJ, we found the in focus edges of the shell and measured the projected thickness as 3792 ± 108 nm. The uncertainty of the measurement comes from the size of one pixel. So the thickness at the top plane of the shell is: $T = 3792$ nm $\times \cos(81°) = 593 \pm 20$ nm.
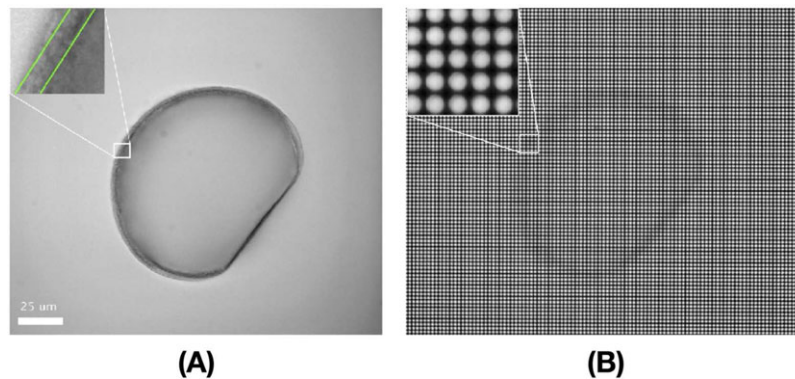
Fig. 3. Images of a 3-day-old clamshell recorded with a bright field microscope equipped with a $60\times/1.4$ NA objective lens and matching condenser optics, and (A) a conventional camera (Hamamatsu ORCA Flash4.0) or (B) a light field camera (specs described in 'Light field LC-PolScope' section). The shell partially absorbs and scatters the light that passes through it and its image appears dark against a bright background. The inset in (A) shows a magnified and contrast enhanced portion of the shell, with two green lines drawn by hand to identify the outer and inner surface of the shell. The inset in (B) is an enlarged portion showing the intensity behind 5×5 microlenses with applied contrast enhancement.
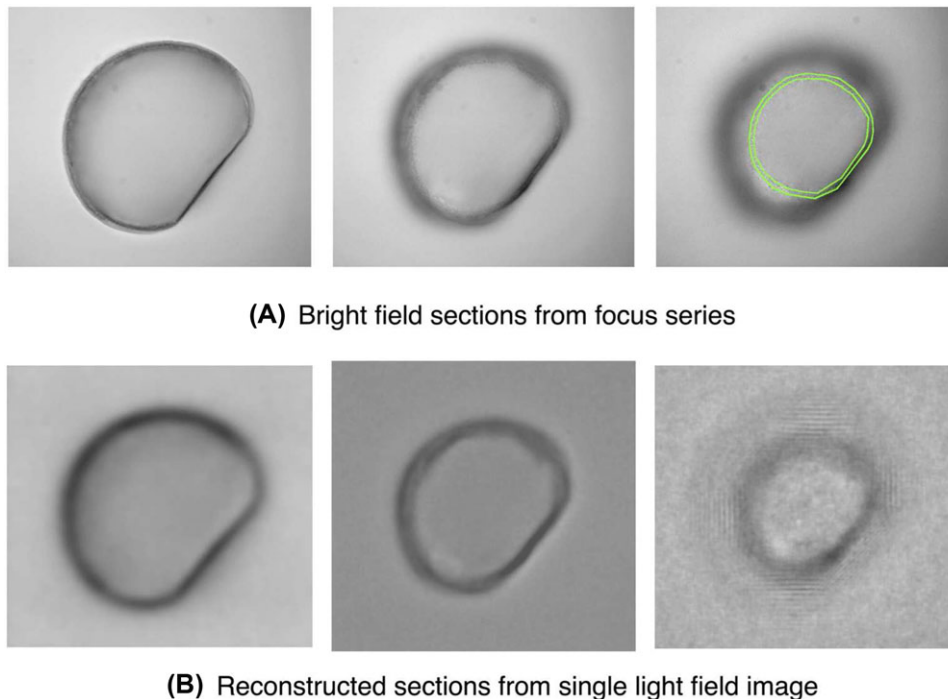

Fig. 4. (A) Optical sections through the juvenile clamshell of Figure 3(A) recorded with the bright field microscope and conventional camera. The green lines drawn by hand in the right most panel outline the fine absorption details that define the shell's cross section at that focus plane (see main text). Note that the dark ring outside the green outline represents out of focus information and not the shell's cross section at that focus plane. (B) Optical sections reconstructed from a single light field image (Fig. 3B) of the shell using the deconvolution method of Broxton *et al.* (2013). Due to the rectification step in the deconvolution method, the shell is rotated by a small angle. The optical sections reconstructed from the light field image do not contain fine absorption details from inside the cross section, but present the in focus part of the shell's cross section at lower resolution without dominant out of focus features. Light field imaging trades some lateral resolution for axial resolution and the ability to reconstruct the 3D shape of the shell.

Observation with the scanning electron microscope

The shell of *M. mercenaria* (hard clamshell) is mineralized by aragonitic crystals that nucleate and grow in an organic matrix (Wilbur & Watabe, 1963; Taylor *et al.*, 1973; Thorn *et al.*, 1995). The formation of the organic matrix and nucleation of the aragonitic crystals control their orientation with respect to the overall shape of the shell (Tiwari & Gallager, 2003), thus controlling the shell's optical properties. To reveal the type and orientation of crystals inside the shell, we induced epitaxial
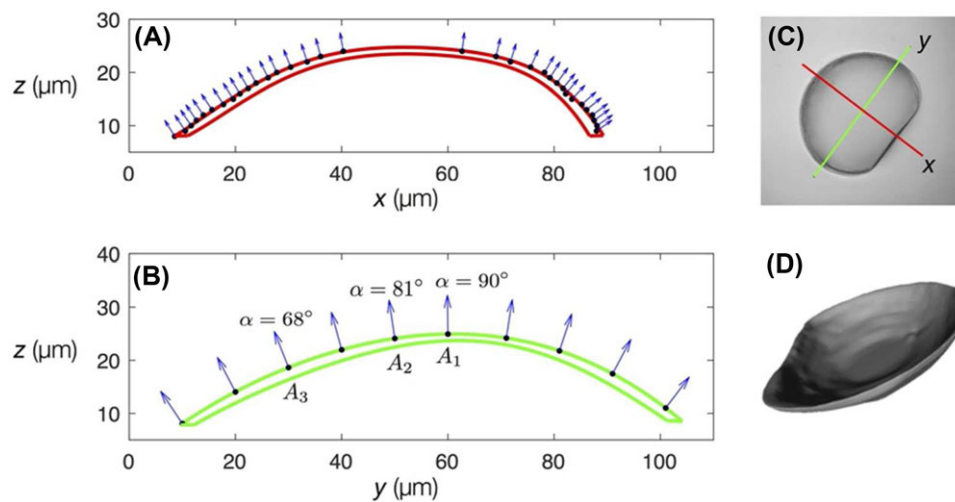
Fig. 5. (A and B) Two vertical cross sections through the shell of Figure 3(A), reconstructed using the complete focus series recorded with the conventional camera. The plane of the cross section is indicated by the green and red line in (C) and includes in both cases the microscope axis, which runs vertical in (A) and (B). The blue arrows in (A) and (B) are normal to the shell surface, which is the inclination angle of the normal. Points A1 and A3 indicate locations of microlenses that are further examined in Figure 10. (D) 3D printable model of 3-day-old juvenile clamshell reconstructed from light microscopy data.
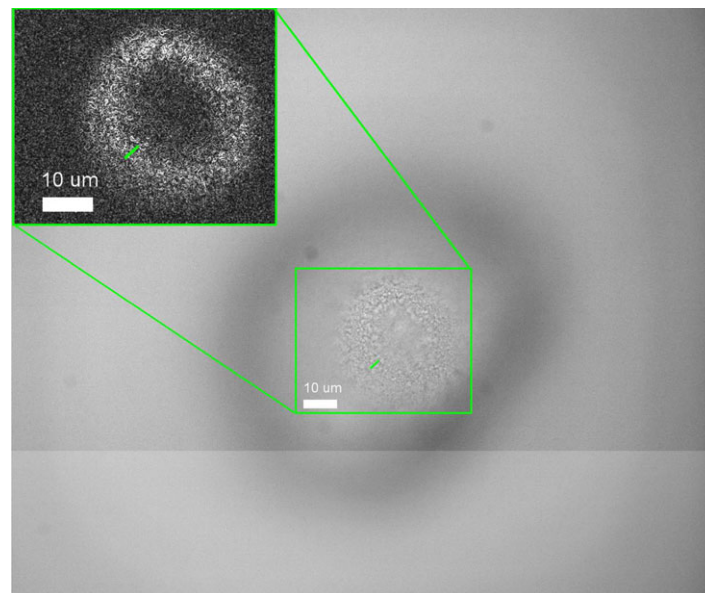

Fig. 6. Conventional bright field image of the shell at a focus plane close to its top. (Inset) The shell cross section was enhanced using the edge detection function of 'ImageJ'. The green line is the shell's thickness projected into the focus plane.

growth of calcium carbonate crystals on the surface of shells, as described in 'Epitaxial crystal growth on juvenile clamshells' section. This experiment was inspired by the work of Okazaki and Inoué (1976) on sea urchin spicules. Figure 7 shows SEM images of an untreated shell, and a shell with epitaxial growth of calcium carbonate crystals. In Figure 7(A), the image of the original shell does not provide any clue about the type and orientation of crystals inside the hard clamshell, while their morphology and alignment are shown clearly in Figure 7(B). In particular, we can observe the pseudo-hexagonal morphol-

ogy of crystals that were seeded by the crystalline material inside the shell. This morphology is compatible with an aragonitic crystal type for the hard clamshell (Bragg, 1924b; de Leeuw & Parker, 1998). In addition, the more important observation here is that the long axes of the pseudo-hexagonal crystals seem to be aligned perpendicular to the surface of the shell. Since the long axis is also the optic axis of the birefringent aragonite crystal (Bragg, 1924b), we expect the optic axis of the shell material to be nearly perpendicular to the shell's surface.
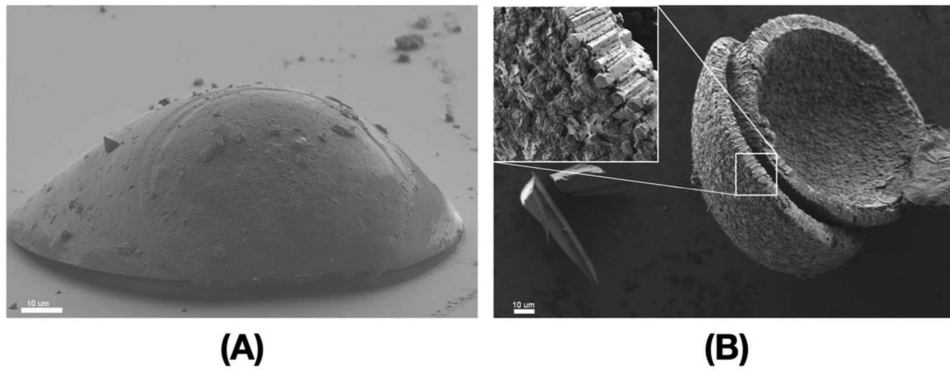
Fig. 7. (A) SEM image of the original shell does not give any hint about the crystallinity of the shell material. (B) SEM image of 3-day-old clamshells treated for epitaxial growth of calcium carbonate on their surfaces. The inset shows the morphologies of the epitaxially grown single crystals and their alignment revealing the structure of the original biocrystals in the shell.

Analysis of the optic axis of clamshells using light field LC-PolScope

Aragonite is a negatively birefringent, biaxial crystal in which the three refractive indices for light polarized along the principal crystallographic axes are different from each other: $n_\gamma = 1.530$, $n_\alpha = 1.686$ and $n_\beta = 1.681$. The acute bi-sectrix is parallel to the crystallographic c-axis and is an axis of pseudo-hexagonal symmetry (Bragg, 1924a). Because the two higher refractive indices are almost equal and significantly higher than the third index value, the angle between the two optic axes is small (18°) and the axes are nearly parallel to the crystallographic c-axis. Moreover, based on the epitaxial growth experiments with results shown in Figure 7, we expect the crystallographic c-axis to be perpendicular to the surface of the shell. The crystallographic a and b axes, however, do not seem to be aligned to each other throughout the thickness of the shell, giving the shell material the appearance of a uniaxial birefringent crystal in our optical experiments. Therefore, we approximate the shell material as a uniaxial crystal with $n_o = 1.530$, $n_e = (1.686 + 1.681)/2 = 1.684$, $\Delta(n) = n_o - n_e = -0.154$, and the optic axis parallel to the pseudo-hexagonal or long axis of the aragonite crystals (Bragg, 1924a).

Since the LC-PolScope equipped with a standard camera only measures the two-dimensional projection of the 3D optical anisotropy, it is not capable of determining the inclination angle of the optic axis of birefringent materials. To reveal the optic axis orientation, we recorded light field images of the same shell at different focus planes and present the images in Figure 8. The aperture images behind each microlens clearly reveal the orientation of the optic axis by mapping the retardance as a function of the tilt angle of rays passing through the shell material at each microlens location.

For example, in Figure 8, the light field image with the focal plane near the top of the shell and its inset of aperture images demonstrate that rays focused in the centre of the aperture carry no retardance, whereas rays focused near the edge of the aperture carry significant retardance. This clearly reveals the optic axis of the shell material at that location as being parallel to the microscope axis. Aperture images recorded at lower focus planes and picked from shell regions that are in focus demonstrate the gradual tilt of the optic axis away from the microscope axis as the shell bends downwards.

For a more quantitative evaluation, we establish the formula to calculate the retardance of a hard clamshell. The total retardance picked up by a ray passing through a uniaxial birefringent sample is determined by three factors: (1) The angle between the ray direction and the optic axis, (2) the physical path length of the ray inside the sample and (3) the sample's birefringence ($n_e - n_o$).

For a sheet like material such as the shell, the retardance Δ imparted on a ray after passing through the sheet is determined by:

$$\Delta = \frac{t}{\cos\varepsilon}(n_e - n_o)\sin^2\beta \,, \tag{1}$$

where t is the thickness of the sheet, ε is the angle of the ray with respect to the normal of the sheet, and β is the angle between the ray and the optic axis. The term $t/\cos\varepsilon$ refers to the physical path length that increases with the tilt angle between the ray and the normal to the sheet, whereas the term $(n_e - n_o)\sin^2\beta$ refers to the increase in birefringence as the ray direction tilts away from the optic axis. In the special case where the optic axis is perpendicular to the shell surface (Fig. 9), the angles β and ε are equal, and Eq. (1) can be rewritten as:

$$\Delta = \frac{t}{\cos\beta}(n_e - n_o)\sin^2\beta. \tag{2}$$

In a microscope, ray directions in object space are described by the ray's tilt angle γ with respect to the microscope axis and its azimuth angle θ in the focus plane. The geometric relationship between the angles β, γ, θ, and the inclination angle σ and azimuth angle Φ of the optic axis leads to an

Bottom focus plane   **Middle focus plane**   **Top focus plane**
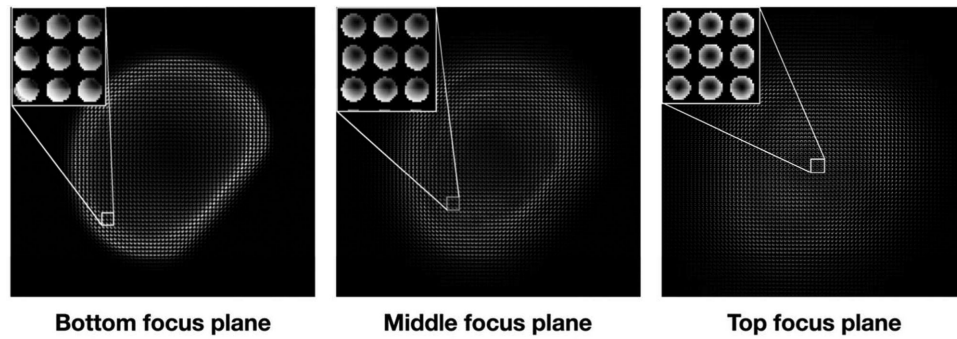
Fig. 8. Light field retardance images with the nominal focus plane near the bottom, middle and top of the shell. The insets in the top left corners are magnified aperture images projected by an array of 3×3 microlenses chosen from shell regions that are in the respective focus plane and correspond to locations marked A1–A3 in Figure 5. The aperture images illustrate the incremental translocation of the retardance minimum to the edge of the aperture, caused by the increasing tilt of the optic axis away from the microscope axis. The magnified images are contrast enhanced.

Table 1. The thickness of shells of different age measured near the top plane using two methods.

Shell's age	Polarized light field method	Conventional method
Two-day old	449 ± 42 nm	503 ± 24 nm
Three-day old	533 ± 41 nm	594 ± 20 nm
Four-day old	1157 ± 167 nm	1146 ± 46 nm

expression for $\cos \beta$ that was first worked out by Oldenbourg (2008):

$$\cos\beta = \cos\theta \cos\sigma \cos\phi \sin\gamma + \cos\gamma \sin\sigma$$
$$+ \cos\sigma \sin\gamma \sin\theta \sin\phi. \qquad (3)$$

The retardance patterns in aperture images such as shown in the insets of Figure 8 can be subjected to a fitting procedure to estimate the parameters of shell thickness, inclination and azimuth angles. In a first step, we calibrated the aperture images that are projected by the microlenses onto the camera sensor in terms of the tilt angle γ of a ray in object space and its radius position in the aperture image (see the Supporting Information). Then we modelled the retardance pattern in the aperture by relating aperture positions (r, θ) to ray directions (γ, θ) in object space, the sheet thickness t, its birefringence $(n_e - n_o)$, and optic axis orientation (σ, Φ). Using nonlinear regression, we varied and found optimal values for the three parameters (σ, ϕ, t) until the simulated retardance images represented a best match with the experimental retardance patterns of selected aperture images. Figure 10 shows the experimental and simulated retardance of one aperture image at the top focus plane and middle focus plane of the shell. The fitting procedure yielded optimized parameters, $(\sigma, \phi, t) = (88°, 164°, 530 \text{ nm})$ and $(68°, 247°, 450 \text{ nm})$. This result confirmed our previous observations that the optic axes of the crystals are perpendicular to the shell surface that are identified as points A_1 and A_3 in Figure 5(B). After applying the fitting procedure

on the 3×3 aperture images in the insets of Figure 8 at the top focus plane, we found similar inclination angles for adjacent sampled areas with an angular standard deviation of about $2°$. This standard deviation is partially caused by statistical variations and partially caused by a systematic change in inclination angle of $1.4°$ due to the curvature of the clamshell. In addition, we averaged the clamshell thickness over the same 3×3 aperture images and found an average thickness of 533 ± 41 nm for this 3-day-old shell.

The shell thickness derived from our retardance measurements is in good agreement with the thickness determined by the bright field method described in 'Three-dimensional shape reconstruction' section.

We then applied the same analysis to 2- and 4-day-old shells, compared their thicknesses near the top plane using both methods, and again found close agreement (see Table 1)

From the data in Table 1, it is apparent that shell thickness increases moderately from day 2 to 3, but does so dramatically between day 3 and 4, and any older samples became too thick to be measured with the polarized light field method.

In Figure 11, we show aperture images and line plots of retardance values measured for 2-, 3-, and 4-day-old clamshells and wish to draw attention to the retardance measured in the minima located near the centre of the aperture. As most apparent for the 4-day-old clamshell, this retardance does not reach zero, but remains finite. This observation can be explained by the fact that the clamshell includes aragonite crystals that are biaxial crystals. Since the retardance of a single biaxial crystal has two minima in directions that are close to the crystallographic c-axis, and it seems that crystalline subregions in the shell are orientationally disordered around the c-axis, the retardance along directions near the c-axis never attain zero and remain finite because of the averaging within a resolved specimen volume. In thinner shells, this effect might be masked by the retardance sensitivity (~ 1 nm) of our method or, more interestingly, might indicate a transition from a calcite to an aragonite crystal structure in nascent clamshells.
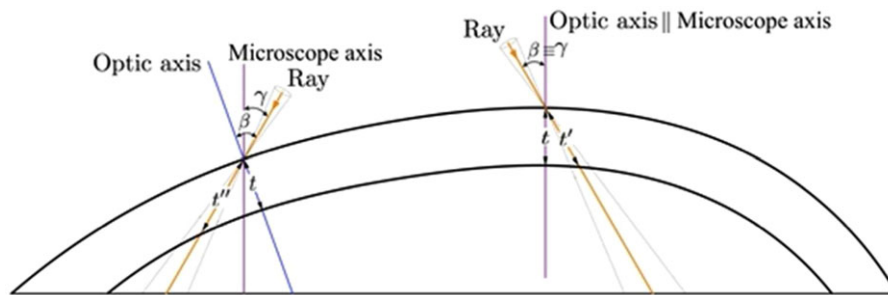
Fig. 9. Sketch of a juvenile clamshell illustrating the relationship among the optic axis, the light ray and the microscope axis. The optic axis is assumed to be parallel to the normal of the shell with thickness t; t' and t'' are physical path length of the ray at considered points.

Diattenuation

We used the LC-PolScope to measure birefringence parameters of the clamshell material. The technique is known to be sensitive to diattenuation as well (Mehta *et al.*, 2013). Since there is measurable attenuation of the light that passes through the shell, as demonstrated by the bright field images in Figures 3, 4 and 6, we examined hard clamshells for diattenuation, that is polarization dependent attenuation that could affect our retardance measurements. Using a setup described by (Mehta *et al.*, 2013) for measuring diattenuation, we found no measurable diattenuation in the shell material, except near the very edge of the shell, where some of the illumination and image rays propagate tangentially to the shell surface. Because diattenuation was confined to areas near the edge where grazing incidence is likely to cause polarization dependent scattering on surface roughness, the reported retardance values for more centrally located shell areas are not affected by diattenuation.
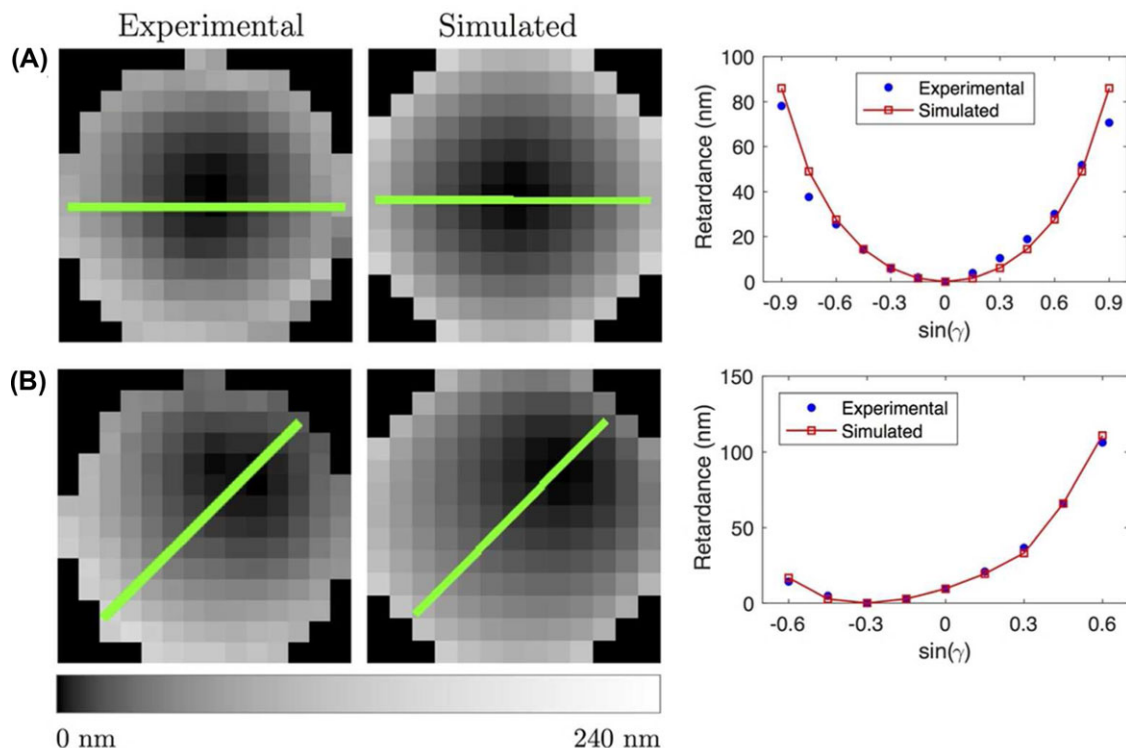

Fig. 10. The experimental and simulated retardance conoscopic images and retardance profiles along green lines: (A) $(\sigma, \Phi, t) = (88°, 164°, 530\ \text{nm})$; (B) $(\sigma, \Phi, t) = (68°, 247°, 450\ \text{nm})$. The blue dots in the graphs represent experimental retardance values in angular steps of about 9°, the red lines represent simulated retardance values. In all four grey scale patterns, white represents 240 nm retardance and grey values are contrast enhanced using a logarithmic look-up-table.
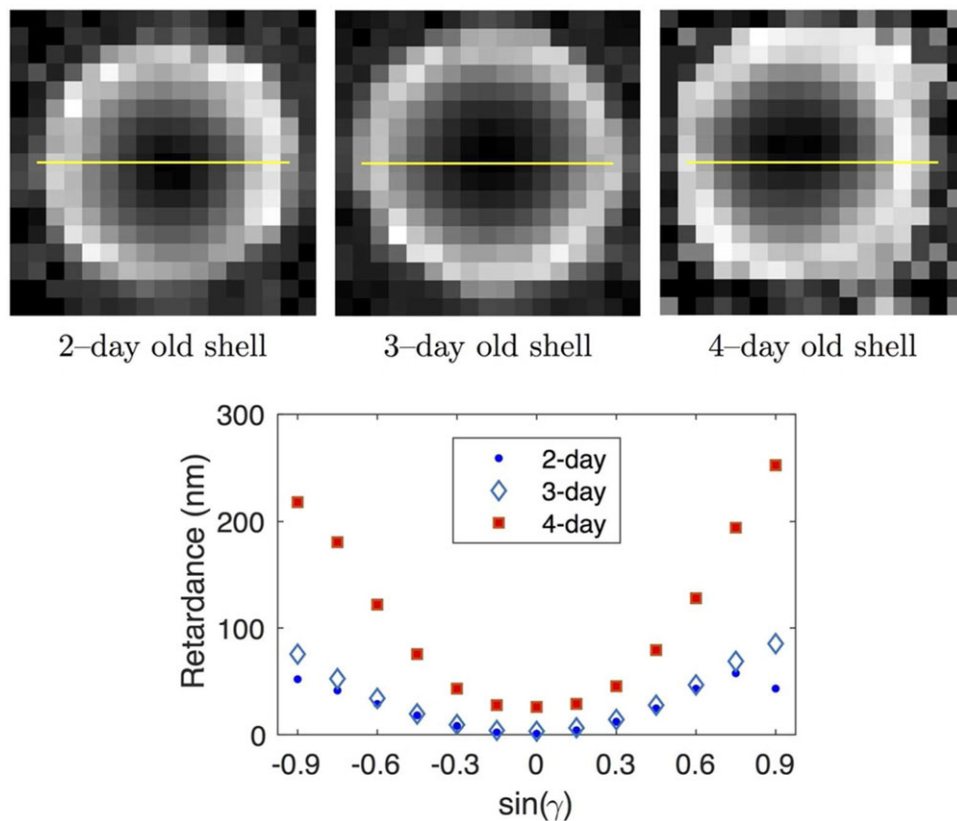
Fig. 11. (Top row) The retardance aperture images of shells focused near their top plane with the darkest spot at the centres of the microlenses of 2-, 3- and 4-day-old clamshells, respectively. (Bottom) Plot profiles of retardance measured along horizontal yellow lines shown in top row illustrating the increase of retardance with age and the finite retardance (∼30 nm) measured in the minimum of the 4-day-old shell.

Discussion

The work reported here is the first application of polarized light field microscopy to map the optic axis and birefringence of objects that have a true, 3D shape, unlike thin, straight calcite films, previously analysed by this method (Oldenbourg, 2008). Ultimately, our work is aimed at analysing even more complex, 3D dynamic scenes using the same experimental setup and type of light field images, but paired with tomographic reconstruction algorithms. Although clamshells represent 3D objects, the reconstruction of their birefringence parameters (optic axis and birefringence $n_o - n_e$) does not require tomographic approaches, because light rays that pass through the sample encounter only once a birefringent sheet. In more complex structures, light rays that pass through the sample and contribute to the retardance and slow axis orientation measured in a given image point will usually traverse several structural elements that each have a different optic axis orientation and birefringence value. The current work aims to establish a simple model that can be used to develop and test more complex reconstruction algorithms. To simplify the current analysis of light field images further, we examined only those aperture images, which sampled the portion of the clamshell that was in the nominal focus plane in a given light field image.

Furthermore, the aragonite crystal layers were approximated as a single uniaxial birefringent layer. Our results indicate that at a young age, this approximation holds well for clamshells

Our current polarization analysis of clamshell birefringence is built on ray optics, evaluating the retardance of rays that passed through the clamshell at different locations and at different inclination angles, as recorded in light filed images. This ray optic interpretation of light field images limits their spatial resolution to the size of a microlens (125 μm) divided by the magnification of the objective lens (60×), equalling 2 μm. Our results justify this approach, as the measured optic axis orientation, thickness, and birefringence of the clamshell varies smoothly and measurably only over longer distances.

In addition to establishing a test model for developing tomographic reconstruction algorithms for birefringence imaging, we hope that our results will facilitate the studies of shells in determining their morphology, especially their thickness as a function of age, and in revealing abnormalities in shell development during environmental stresses. Ultimately, we work

to extend the applications of our approach to structural studies in biology, physics, chemistry, medical and material science.

Acknowledgements

References

Bragg, W. (1924a) The refractive indices of calcite and aragonite. *Proc. R. Soc. Lond. A* **105**(732), 370–386.

Bragg, W. (1924b) The structure of aragonite. *Proc. R. Soc. Lond. A* **105**(729), 16–39.

Broxton, M., Grosenick, L., Yang, S., Cohen, N., Andalman, A., Deisseroth, K. & Levoy, M. (2013) Wave optics theory and 3-D deconvolution for the light field microscope. *Opt. Express* **21**(21), 25418–25439.

de Leeuw, N.H. & Parker, S.C. (1998) Surface structure and morphology of calcium carbonate polymorphs calcite, aragonite, and vaterite: an atomistic approach. *J. Phys. Chem. B* **102**(16), 2914–2922.

Levoy, M., Ng, R., Adams, A., Footer, M. & Horowitz, M. (2006) Light field microscopy. *ACM Transactions on Graphics (TOG)* (ed. by Karita Bala), vol. **25**, pp. 924–934. ACM, Boston, MA.

Mehta, S.B., Shribak, M. & Oldenbourg, R. (2013) Polarized light imaging of birefringence and diattenuation at high resolution and high sensitivity. *J. Opt.* **15**(9). http://doi.org/10.1088/2040-8978/15/9/094007.

Okazaki, K. & Inoué, S. (1976) Crystal property of the larval sea urchin spicule. *Dev. Growth Differ.* **18**(4), 413–434.

Oldenbourg, R. (2008) Polarized light field microscopy: an analytical method using a microlens array to simultaneously capture both conoscopic and orthoscopic views of birefringent objects. *J. Microsc.* **231**(3), 419–432.

Oldenbourg, R., Inoué, S., Tiberio, R., Stemmer, A., Mei, G. & Skvarla, M. (1996) Standard test targets for high resolution light microscopy. *Nanofabrication and Biosystems: Integrating Material Science, Engineering and Biology* (ed. by H. C. Hoch, L. W. Jelinsky & H. Craighead), pp. 123–138. Cambridge University Press, Cambridge, England.

Taylor, J.D., Hall, A. & Kennedy, W.J. (1973) *The Shell Structure and Mineralogy of the Bivalvia,* [Part] *II: Lucinacea-Clavagellacea Conclusions.* Trustees of the British Museum (Natural History).

Thorn, K., Cerrato, R.M. & Rivers, M.L. (1995) Elemental distributions in marine bivalve shells as measured by synchrotron X-ray fluorescence. *Biol. Bull.* **188**(1), 57–67.

Tiwari, S. & Gallager, S. (2003) Machine learning and multiscale methods in the identification of bivalve larvae. In ICCV, 494–501.

Wilbur, K.M. & Watabe, N. (1963) Experimental studies on calcification in molluscs and the alga coccolithus huxleyi. *Ann. N.Y. Acad. Sci.* **109**(1), 82–112.

Supporting Information

Additional supporting information may be found online in the Supporting Information section at the end of the article.

Supporting Information

Supplemental information

The intent of this supplemental information is to describe our procedure to calibrate the aperture images that are projected by the microlenses onto the camera sensor.

Each disk-shaped aperture image is contained within 17x17 camera pixels, it has a center and a radius r_{NA} that corresponds to the NA of the microscope objective lens. Any point in the disk with radius $r < r_{NA}$ is the focus of parallel rays that have a tilt angle γ in object space that is calculated using:

$$\gamma = \arcsin((r \times NA)/(r_{NA} \times n)) \qquad [4]$$

with n the refractive index of the immersion medium. Equation [4] is an expression of the Abbe sine condition used in the objective lens design. Hence, for calculating the angle γ from a position with radius r from the center, it is necessary to know r_{NA}. Because of the poor pixel resolution, the true edge of the aperture image is not readily discernable. Furthermore, in transmitted light microscopy, the aperture of the objective is not necessarily fully illuminated because of partial vignetting or stops in the illuminating beam. Therefore, we have used the diffraction of line gratings of known periodicities to calibrate the positions in the aperture image with their corresponding tilt angles of rays in object space. Line gratings placed in the object plane are resolved in the image if at least their zero and first diffraction orders are captured by the microscope objective lens [Oldenbourg and Shribak, Handbook of Optics]. The relationship of the angle γ between the zero and first diffraction order, the pitch d of the grating, and the wavelength λ of the light is:

$$d \times \sin(\gamma) = \lambda/n \qquad [5]$$

with n the refractive index of the medium surrounding the grating ($n = 1.52$ in our experiments). The distance r in the aperture plane between the zero and first orders is directly related to the diffraction angle γ of the grating:

$$r = const\ \sin(\gamma) \qquad [6]$$

The value of $const$ is the subject of the calibration and will be expressed in units of pixel representing a distance.
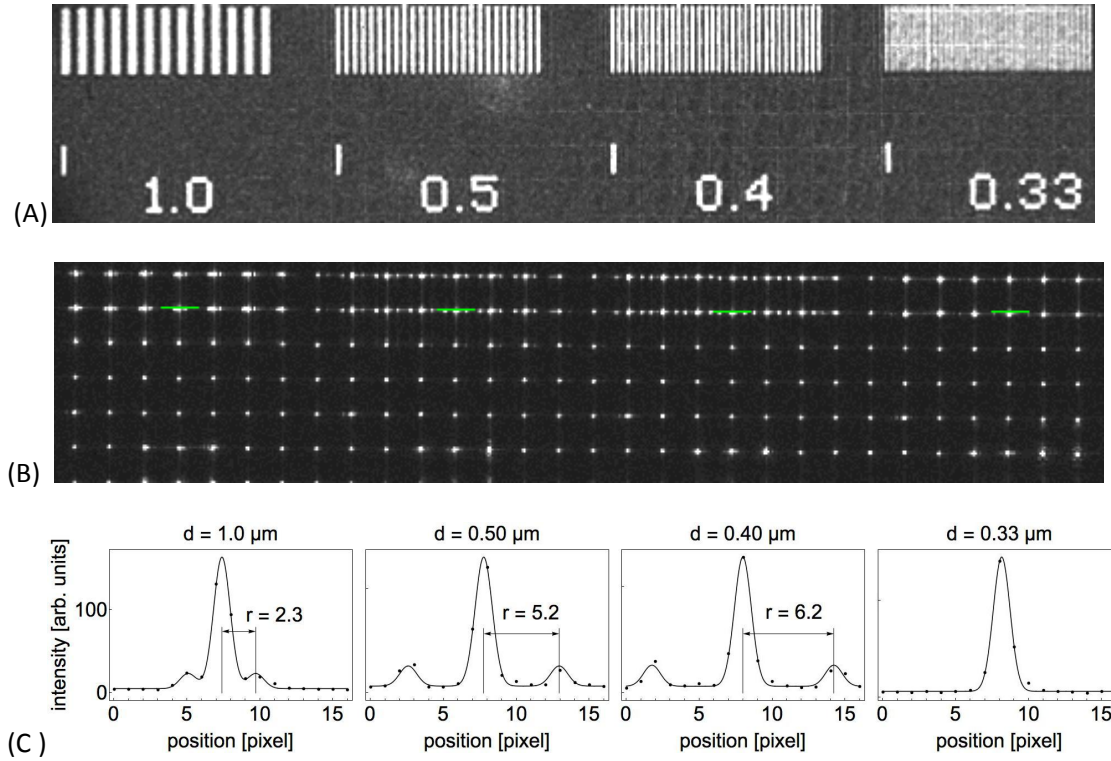
Figure 12: Line gratings of the MBL/NNF test target, imaged with (A) standard and (B) light field microscope. In B, the collimated illumination beam, i.e. condenser aperture nearly closed, is imaged into the center of the aperture, while the first order diffraction is visible in two subsidiary maxima. The horizontal green lines identify the pixels whose recorded intensities are shown as data points in the profiles of panel C. The continuous lines in the graphs of C represent the best fit applied to the data to determine the distance r between the central and subsidiary maxima.

For the calibration, we have used the well defined MBL/NNF test target that consists of a glass coverslip with a thin aluminum layer, in which fine line gratings were etched using electron lithography [Oldenbourg et al., in Nanofabrication and Biosystems]. **Fig. 12A** shows line gratings with periodicities between 1.0μm and 0.33μm, which were imaged with the same setup as the shells described in the main text of the article, using light of wavelength 482 nm. **Fig. 12B** shows light field images of the same gratings, with the microlenses in the position that projects the back aperture images onto the camera sensor. To make the diffraction patterns visible, the gratings were illuminated with a highly collimated beam by nearly closing the diaphragm in the aperture of the condenser lens. The top two rows of aperture images in panel B show the diffraction maxima of the gratings whose images fall on the respective microlenses. **Fig. 12C** shows horizontal intensity profiles along lines that are indicated in green in panel B. The intensity profiles clearly show a central maximum and 2 subsidiary maxima symmetric in position to the central one and increasing in distance with decreasing grating pitch. Only the diffraction pattern of the 0.33μm grating does not show first order maxima, because its diffraction angle of 73° is outside of the acceptance angle of 67° of the oil immersion objective with 1.4 NA.

The continuous lines in the graphs of **Fig. 12C**, represented the best fit using least square regression of the data points to a sum of three Gaussian curves, one representing the central line and two, spaced symmetrically to the central line, representing the first order diffraction maxima. For each line grating there were 10 aperture images, i.e. 10 microlenses that covered the grating,. This allowed us to determine the mean and standard deviation of the measured distance r. The linear fit through the data points in the graph of **Fig. 13** gave the measured value of *const* = 7.93 [pixel] in expression [6] and the radius r_{NA} = 7.25 that corresponds to the acceptance angle of the objective lens that we used in our experiments.
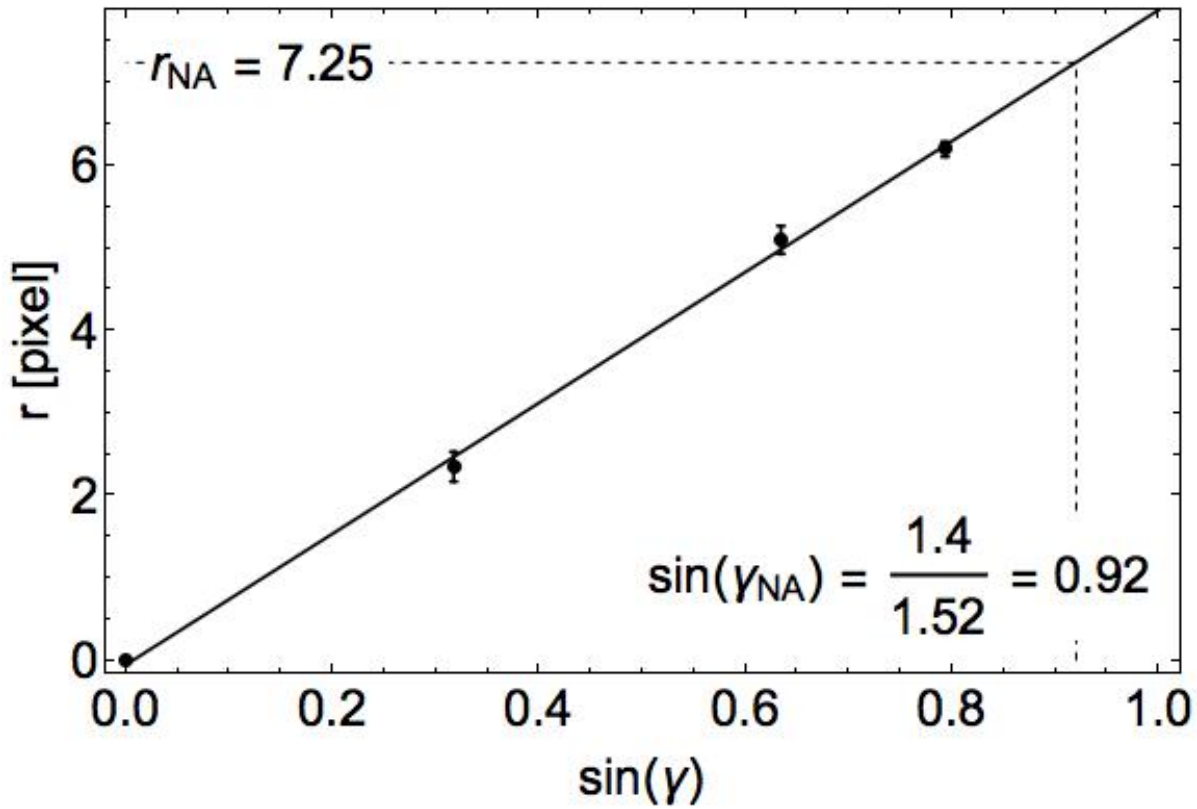

Figure 13: Graph representing the measured distance *r* between zero and first diffraction maxima (see **Fig. 12C**) and the diffraction angle γ derived with expression [5]. Data points and error bars represent means and standard deviations of 10 measurements each. r_{NA} is the aperture radius used in the calculations of the optic axis inclinations presented in the main text.